Indian Journal of Pure & Applied Physics
Vol. 61, June 2023, pp. 568-588
DOI: 10.56042/ijpap.v61i7.109

Visible to Infrared Dielectric Metasurfaces and their Applications

Shubhanshi Sharma[a]*, Monica Pradhan[b], Anjali Yadav[a] & Shailendra K Varshney[a]*

[a]Department of Electronics and Electrical Communication Engineering, Indian Institute of Technology Kharagpur, 721 302, India
[b]School of Nanoscience and Technology, Indian Institute of Technology Kharagpur- 721 302, India

Received 1 November 2022; accepted 12 June 2023

Dielectric metasurfaces, two-dimensional variant of metamaterials, have received significant attention from the scientific community due to enormous potential and ability to cater to various spectral bands of the electromagnetic spectrum and pave the way to achieve multi-functionalities in a single device, which was not possible earlier. Dielectric metasurfaces have the edge over their metallic counterparts in terms of zero-ohmic propagation losses, high efficiency, or ultra-high-quality factor and are compatible with existing CMOS technology. They support both electric and magnetic resonances in the optical domain. Here, we provide a comprehensive review of dielectric metasurfaces, encompassing visible to far-infrared wavelength regions, and discuss selective applications which may find its commercial value in the near future. Finally, we provide an outlook and perspective on dielectric metasurfaces for nonlinear and quantum applications.

Keywords: Metamaterials; Dielectric metasurfaces; Quantum technology; Zero-Ohmic propagation loss

Introduction

Light-matter interaction has been the heart of most optical devices and applications. When a light signal in the form of plane-wave is incident on a particle of any shape and material and whose size is smaller than the diffraction limit, electric and magnetic multipoles are induced that give rise to the scattering of light. To understand such light-matter interaction, a scattering theory was developed long back and still is the subject of study, including the present times[1]. One of the successful applications and studies in the last few decades have been the metamaterials which may exist in one-, two- or three-dimensional forms and can be made from all materials such as metals, dielectrics, semiconductors, and superconductors.

Metamaterials are artificially engineered to exhibit properties such as negative refractive index[2], superlensing[3], hyperspectral imaging[4], inverse doppler effect[5], cloaking[6], perfect absorption[7], wave-front manipulation[8], and nonlinearity[9] that cannot be found in traditional optical devices. The two-dimensional equivalent of metamaterials is popularly known as metasurfaces, which are easier to fabricate as compared to their three-dimensional counterpart[10]. Metasurfaces, on the basis of materials, can be divided into two categories: plasmonic metasurfaces and dielectric metasurfaces. Plasmonic metasurfaces are made of metals such as Gold (Au), Silver (Ag), Aluminum (Al), or highly degenerate semiconductors (n-type, p-type Silicon (Si)),where the working principle mechanism isbased on surface plasmon resonances (SPR) or localized surface plasmon resonances (LSPR) due to the generation of oscillating free electrons, known as plasmons[11,12]. Owing to its metallic nature, the metallic metasurface poses high ohmic losses, strong dispersion, and low-quality factor (Q). To circumvent these issues, researchers have explored dielectric metasurfaces made up of high to moderate refractive index materials such as Si, Germanium (Ge), Gallium Arsenide (GaAs), Titanium dioxide (TiO_2) and so on, where simultaneous excitation of electric and magnetic resonances takes place due to the oscillation of polarized charges that induce the circular displacement current in metasurface[13,14]. Explosive growth is seen in this domain due to the precise manipulation of amplitude and phase of propagating optical waves. The most prominent advantage of using metasurface is to provide a desired phase gradient in the range of 0 to 2π that felicitates control over amplitude, polarization and wave-vector[15,16].

Over the past decade, extensive research has been done in the field of dielectric metasurface due to many advantages over their metallic counterpart, such as: (i) low radiative losses in the optical region, (ii) ease of fabrication as dielectric materials are compatible with the existing CMOS technology,

*Corresponding author:
(E-mail: shubhanshi07@iitkgp.ac.in; skvarshney@ece.iitkgp.ac.in)

(iii) high efficiency due to high Q factor, and (iv) resonance properties are geometry dependent rather than material. Fig. 1(a) shows the number of articles published in the last few years, which clearly indicates significant interest among the scientific community in the dielectric metasurface.

In this article, we present a comprehensive overview of the theory and recent research advancement in dielectric metasurface, with a focus on selective applications such as metalens, beam steering, meta-holograms, all-dielectric biosensors, and metasurface integration with optical fibers, as depicted in Fig. 1(b). This review article starts with the background and the basic understanding of dielectric resonators, followed by the applications of metasurfaces in various fields. The integration of dielectric metasurface with two-dimensional materials has also been described. Finally, we provide an outlook and perspectives on dielectric metasurfaces in various research domains such as quantum, agro-food, energy and healthcare.

2 Background and Fundamental Concepts

Historically, many physicists have carried outnotable work in this field and concluded that scattered light is polarized, viz., Tyndall considered the size of the particle and explained to attain the linearly polarized light when the incident optical beam and scattered beam are perpendicular to each other[17]. Later on, Rayleigh stated that the particle size should be small compared to the incident light wavelength. Therefore, in elastic scattering, the incident and scattered radiations have the same frequency, which is the case in Rayleigh scattering, governed by $1/\lambda^{4,}$ where λ is the incident wavelength. This also set an equivalence with the oscillating multipoles. Fundamentally, scattering is defined as the radiation scattered from the set of oscillating charges when light is illuminated onto any obstacle[18]. The obstruction can be of any shape and size, but for the understanding of physics, the simplest structure one can think of is the sphere that can be approximated as a point particle[19]. Before Mie, Lorentz contributed to establish the precise solution of scattering from a spherical particle. In 1908, Mie published his seminal paper giving a comprehensive study of quasi-elastic interaction between the sphere and electromagnetic waves. The beauty of the Mie formulation is its applicability to non-spherical particles as well. The exact solution can be found using Maxwell equations. Rayleigh used the method of partial wave analysis for determining the scattering of light in all directions, while Mie formulated his theory by using partial wave decomposition where the incident, scattered, and internal electric fields can be written down independently using spherical harmonics[20] that include both the shape and size along with the material properties of the particle. Both the electric and magnetic scattering amplitudes are calculated using dipole, quadrupole, octupole, and higher-order multipole moments can then be computed. The coefficients are written with respect to x (size parameter) *i.e.*, $x = k\times a = 2\pi aN/\lambda$. Relative refractive index $m = k_1/k = N_1/N$ where N_1 is refractive index of the particle and N is refractive index of medium. Mie coefficients can be written as,

$$a_n = \frac{\mu m^2 j_n(mx)\left[x j_n(x)\right]' - \mu_1 j_n(x)\left[mx j_n(mx)\right]'}{\mu m^2 j_n(mx)\left[x h_n^{(1)}(x)\right]' - \mu_1 h_n^{(1)}(x)\left[mx j_n(mx)\right]} \quad \ldots (1)$$

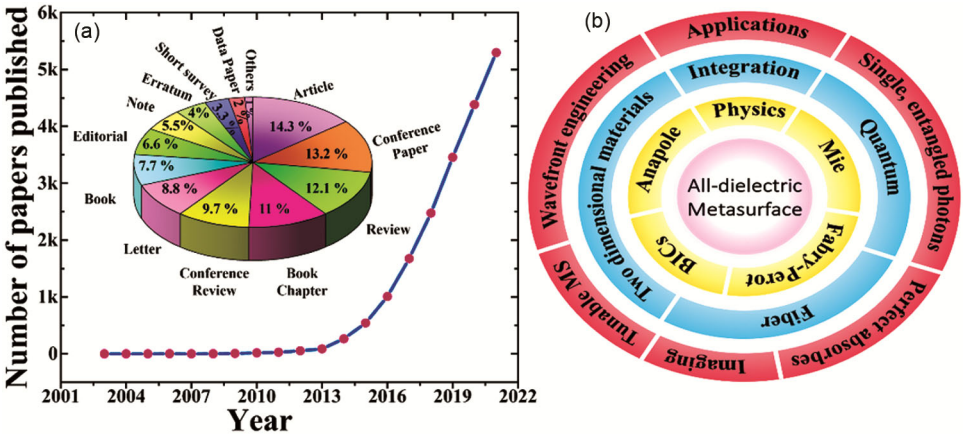

Fig. 1 — (a) Number of articles published in the area of dielectric metasurface (source: Scopus), (b) dielectric metasurface in nut-shell, explaining its physics and various applications.

$$b_n = \frac{\mu_1 j_n(mx)\left[xj_n(x)\right]' - \mu j_n(x)\left[mxj_n(mx)\right]'}{\mu_1 j_n(mx)\left[xh_n^{(1)}(x)\right]' - \mu h_n^{(1)}(x)\left[mxj_n(mx)\right]'} \quad \ldots (2)$$

$$c_n = \frac{\mu_1 j_n(x)\left[xh_n^{(1)}(x)\right]' - \mu_1 h_n^{(1)}(x)\left[xj_n(x)\right]'}{\mu_1 j_n(mx)\left[xh_n^{(1)}(x)\right]' - \mu h_n^{(1)}(x)\left[mxj_n(mx)\right]'} \quad \ldots (3)$$

$$d_n = \frac{\mu_1 m j_n(x)\left[xh_n^{(1)}(x)\right]' - \mu_1 m h_n^{(1)}(x)\left[xj_n(x)\right]'}{\mu m^2 j_n(mx)\left[xh_n^{(1)}(x)\right]' - \mu_1 h_n^{(1)}(x)\left[mxj_n(mx)\right]'} \quad \ldots (4)$$

Here a_n and b_n are the scattering coefficients, c_n, and d_n are the field coefficients inside the particle, and prime denotes the first-order derivative with respect to its argument μ and μ_1 are the permeability of free-space and nanoparticle, h_n is the Hankel function, where as j_n is the spherical Bessel function

For the non-absorbing medium, the rate of light absorption is independent of radius. Further, this theory is extended to the scatterer present in the absorbing medium[21], where the radius of the scatterer becomes essential in calculating the scattering and extinction coefficients which are expressed using the Mie scattering amplitudes. The dependence over the polar and azimuthal angles provides a practical viewpoint for the scattered light by an obstacle[18].

$$S_1 = \sum_n \frac{2n+1}{n(n+1)}\left(a_n \pi_n + b_n \tau_n\right) \quad \ldots (5)$$

$$S_2 = \sum_n \frac{2n+1}{n(n+1)}\left(a_n \tau_n + b_n \pi_n\right) \quad \ldots (6)$$

where, S_1 and S_2 denote the scattering amplitudes related to the polar angle (θ) and the azimuthal angle (ϕ), respectively. With the help of Eqs (5) and (6), it is possible to achieve maximum scattering in a particular direction. Although forward scattering can be attained easily, however, to obtain backward scattering, it becomes relevant to tune the size of particles and other geometrical parameters. In 1976, Kerker and coworkers observed a shift in the frequency due to the geometry and material properties of smaller particles[22,23]. Kerker also proposed the idea of choosing the magnetic sphere and studied the asymmetry in the forward and backward scattering phenomenon[24]. The analysis of multipolar resonances can fulfill the demands of unidirectional scattering[25–27]. In order to understand the scattered field, cartesian multipole decomposition is generally adopted, which can be used in either cartesian or spherical coordinate systems.

In the cartesian multipole decomposition, displacement current is expanded using Taylor series, which provides insight into various multipole moments, such as electric dipole (ED), magnetic dipole (MD), electric quadrupole (EQ), and magnetic quadrupole (MQ). In long-wavelength approximation, the imprints of toroidal components (fundamental and higher-order) are studied and are shown in Table 1. Also, the respective illustration of multipoles with far-field radiation patterns is shown in Table 1. With the help of scattered fields, the exact multipoles can be derived that also validate the Mie solutions, as given in Table 2.

The total scattered power and scattering cross-section can be calculated as,

$$P_{sca} = \frac{k^4 \varepsilon_d^{1/2}}{12\pi\varepsilon_0^2 c\mu_0}\left|p_i + \frac{ik\varepsilon_d T_i^{(e)}}{c} + \frac{ik^3 \varepsilon_d^2 T_i^{(2e)}}{c}\right|^2 + \frac{k^4 \varepsilon_d \varepsilon_d^{1/2}}{12\pi\varepsilon_0 c}\left|m_i + \frac{ik\varepsilon_d T_i^{(m)}}{c}\right|^2 + \frac{k^4 \varepsilon_d \varepsilon_d^{1/2}}{160\pi\varepsilon_0^2 c\mu_0}\left|Q_{ij}^{(e)} + \frac{ik\varepsilon_d T_{ij}^{(Qe)}}{c}\right|^2 + \frac{k^6 \varepsilon_d^2 \varepsilon_d^{1/2}}{160\pi\varepsilon_0 c}\left|Q_{ij}^{(m)} + \frac{ik\varepsilon_d T_{ij}^{(Qm)}}{c}\right|^2 + \cdots \quad \ldots (7)$$

$$\sigma_{\text{sca}} = 2\left(\frac{\mu_0}{\varepsilon_0 \varepsilon_d}\right)^{1/2} \frac{P_{scat}}{\left|E_{inc}\right|^2} \quad \ldots (8)$$

For the dipolar-like particles, the electric and magnetic polarizabilities are either equal for backward scattering or opposite signs for forward scattering. Using the metasurfaces, the simultaneous excitation of electric and magnetic resonances at a particular wavelength gives rise to the Kerker scattering[28], where both the amplitude and phase of the resonating components are considered. If ED is in phase with MD, forward scattering can be achieved. Note that even if higher-order multipolar components are analyzed, the condition for forward scattering remains the same while the amplitude decreases. On the other hand, in optics, one of the complex and difficult problems is diffraction and the challenge to overcome the diffraction limit. Huygen, in 1690, put forward a theory to understand the same. According to Huygens' principle, a point source emits a spherical wavefront, which is referred to as the primary wavefront, and every point in the primary produces secondary wavefronts. Later on, Fresnel also studied the diffraction theory using this principle and concluded that secondary wavelets interfere mutually[29]. Considering Huygens' sources as antennae, the propagation of waves in the far field is always in the forward direction. Therefore, the spectral overlap of electric and magnetic dipolar

Table 1 — Various multipole moments, illustration of multipolar moments, and far-field radiation pattern.

Multipole Moment	Equation		Far-field Radiation Pattern
Electric Dipole (ED)	$\frac{i}{\omega}\int J_i d^3r$		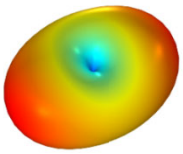
Magnetic Dipole (MD)	$\frac{1}{2}\int (r\times J)_i d^3r$		
Toroidal Electric Dipole (TED)	$\frac{1}{10}\int\left[(J.r)r_i - 2r^2 J_i\right]d^3r$		
Toroidal Magnetic Dipole (TMD)	$\frac{i\omega}{20}\int r^2\left(r\times J\right)_j d^3r$		
Electric Quadrupole (EQ)	$\frac{i}{\omega}\int\left[r_i J_j + r_j J_i - \frac{2}{3}\delta_{ij}(r.J)r_i\right]d^3r$	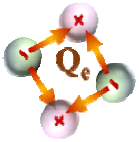	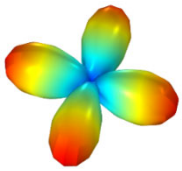
Magnetic Quadrupole (MQ)	$\frac{1}{3}\int\left[\left(r\times J\right)_i r_j + \left(r\times J\right)_j r_i\right]d^3r$		
Toroidal Electric Quadrupole (TEQ)	$\frac{1}{42}\int\begin{bmatrix}4(r.J)r_i r_j + 2(J.r)r^2\delta_{ij}\\ -5r^2\left(r_i J_j + r_j J_i\right)\end{bmatrix}d^3r$	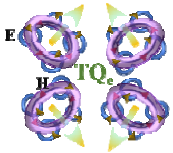	
Toroidal Magnetic Quadrupole (TMQ)	$\frac{i\omega}{42}\int r^2\left[r_j\left(r\times J\right)_p + \left(r\times J\right)_j r_p\right]d^3r$	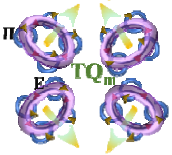	

moments of comparable strengths pave the way to achieve Huygens' metasurface[30] with an ability to control both the cross- and co-polarization radiations for efficient refraction[31]. The metallic nanoparticle has the ability to enhance the light-matter interaction due to plasmonic resonances, which may aid in achieving the directionality of electromagnetic radiation, which helps create nanophotonic devices. The unique and optimized arrangement of the resonator fulfills the demands of unidirectionality in a certain direction, whatever may be the axis of polarization (Fig. 2(b,c)). This leads to the transverse Kerker scattering, where the scattered field is perpendicular to the propagating field while suppressing both the forward and backward scattering (Fig. 2(d)). The limiting conditions for achieving different scattering phenomena, namely, super-scattering, scattering dark state, and Kerker effect, are shown in Fig. 2(a). For a cubic nanoparticle, the study of transverse scattering reveals the aligning of the phase of different multipole moments that can provide directionality in a particular direction, Fig. 2(e). With

Table 2 — Exact multipole decomposition of various multipoles

Multipole Moment	Equation
Electric Dipole (p_α)	$-\frac{1}{i\omega}\left[\int J_\alpha^\omega j_0(kr)\,d^3r+\frac{k^2}{2}\int\left\{3(r\times J_\omega)r_\alpha-r^2J_\alpha^\omega\right\}d^3r\right]\frac{j_2(kr)}{(kr)^2}$
Magnetic Dipole (m_α)	$\frac{3}{2}\int\left[(r\times J_\omega)_\alpha\frac{j_1(kr)}{kr}\right]d^3r$
Electric Quadrupole ($Q^e_{\alpha\beta}$)	$-\frac{3}{i\omega}\left[\begin{array}{l}\int\left\{3\left(r_\beta J_\alpha^\omega+r_\alpha J_\beta^\omega\right)-2(r\bullet J_\omega)\delta_{\alpha\beta}\right\}\frac{j_1(kr)}{kr}d^3r+\\ 2k^2\int\frac{j_3(kr)}{(kr)^3}\left\{5r_\alpha r_\beta(r\bullet J_\omega)-\left(r_\alpha J_\beta+r_\beta J_\alpha\right)r^2-r^2(r\bullet J_\omega)\delta_{\alpha\beta}d^3r\right\}\end{array}\right]$
Magnetic Quadrupole ($Q^m_{\alpha\beta}$)	$15\int\left[\frac{j_2(kr)}{(kr)^2}\left\{r_\alpha(r\times J_\omega)_\beta+r_\beta(r\times J_\omega)_\alpha\right\}d^3r\right]$

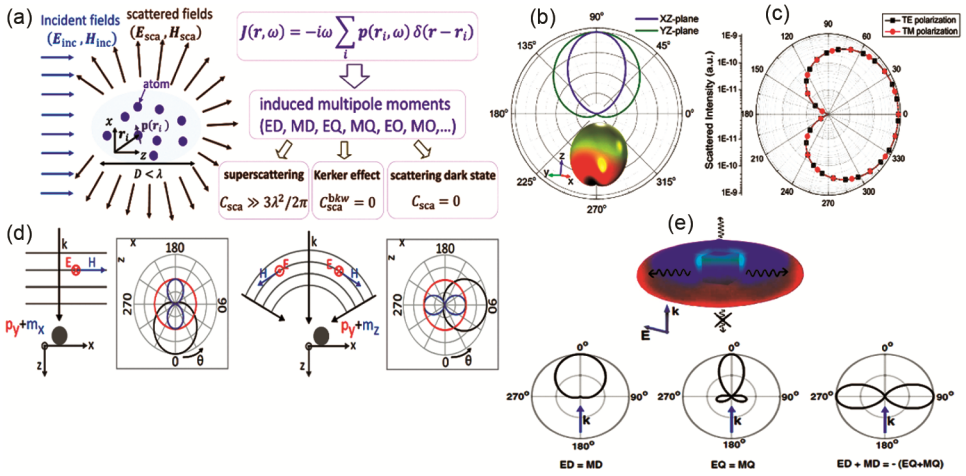

Fig. 2 — Scattering from assorted nanoparticles. (a) Illustration showing the limiting conditions of scattering from a nanoparticle of size D, smaller than the wavelength of incident light. Reproduced with permission[33]. Copyright 2020, American Physical Society. (b) Directivity shown by disk-shaped gap surface plasmon resonance (GSP resonator, *i.e.*, metal-insulator-metal resonator). Reproduced with permission[25]. Copyright 2015,Optical Society of America.(c) Scattering shown for particles with TE and TM polarizations, reproduced with permission[34]. Copyright 2008, Optical Society of America. (d) shows the Kerker scattering and Huygens' dipole. Reproduced with permission[32]. Copyright 2018, American Physical Society. (e) The resonances and the corresponding radiation pattern of cubic nanoparticle are due to transverse scattering of light. Reproduced with permission[28]. Copyright 2019, American Physical Society.

the help of both Huygens's metasurface and Kerker scattering, it is possible to attain either near unity transmission or by suppressing both the forward and the backward scattering in the far-field, one may achieve non-radiating states[28,32] also.

When the size of the scatterer becomes comparable ($D\approx\lambda$) to the incident wavelength or larger than the wavelength ($D>>\lambda$), it is possible to realize various types of scattering phenomena. For example, if the particle size is less than the incident wavelength ($D<\lambda$), Rayleigh scattering dominates. While in the case of Mie scattering, the exact Mie solution exists only for the particles that have geometry nearby to that of spheres, disks, cubes, or long rods. In case the scatterer size is quite large compared to the wavelength, one has to employ a two-dimensional Mie scattering formulation, whereas if the particle size is very small in contrast to the wavelength, then the solution is given by three-dimensional Mie resonance[35].

There is a case where the large aspect ratio of the particle is comparable to that of wavelength, then the hybrid Mie-Fabry Perot (FP) mode is supported by such structures, as illustrated in Fig. 3. In general, FP cavity is comparable to the wavelength of incident light[36]. It consists of partially reflecting mirrors placed parallelly at a distance equal to the operating wavelength. The continuous reflection from both

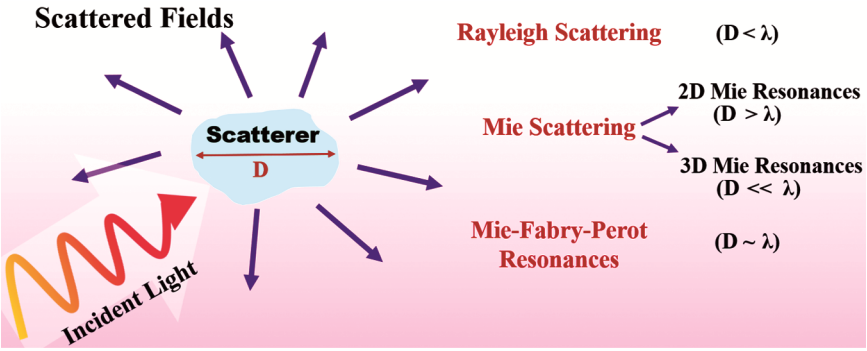

Fig. 3 — Illustration showing the relation between particle size and the different types of resonances.

mirrors gives rise to the forward and backward propagating waves[37]. These waves interfere and form the pattern of standing waves that are useful in creating the laser cavity[38]. Deriving the resonances from the light-matter interaction from the dielectric devices, the FP model is used to describe the leaky modes due to the multiple reflections[39]. It also leads to the strong enhancement of the electric field along with high transmission[40].

All such scattering phenomena can induce various types of resonances, such as Mie, FP, and Fano-resonances, characterized by various line shapes and quality factor. Among these, the most important resonance is the Fano-resonance due to its capability to confine light in nanostructure with a high or ultra-high-quality factor. The interfering resonances can give rise to radiation less modes such as bound states in the continuum (BIC) and anapole with the optimized nanostructure. In 1929, von Neumann and Wigner claimed the existence of embedded eigenstates in the continuum of energy states which can be found by solving the single-particle Schrodinger equation. These states are known as BICs[41,42], the unique light states that remain localized in the continuous spectrum without coupling with the continuum. Also, these states are referred to as trapped mode or embedded eigenvalues. In 1985, Friedrich & Wintgen reported that destructive interference between the two resonances could lead to the avoided resonance crossing that gives rise to the suppression of one resonance, thus transforming into a BIC[41]. The concept of BICs can be found in all the fields of wave systems[42]. The first theoretical analysis of BICs in photonics was reported in 2008 in an array of coupled waveguides[43]. Later in 2011, BICs were experimentally observed in an array of waveguides indicating that BICs are an efficient method to trap electromagnetic fields[44]. BICs may also occur due to the destructive interference of two or more resonant states where radiative losses are entirely suppressed. This type of BICs is known as Friedrich and Wintgen (F-W) resonance[45].

Another way to achieve BICs is to break the symmetry of a structure that induces a coupling between embedded states and continuum. Such resonances are symmetry-protected BICs[46,47]. Apart from the aforementioned approaches, BICs can also be obtained by tuning the geometrical parameters such that the coupling coefficient of a single resonance vanishes. This is known as accidental BICs[48,49]. Ideally, the most significant advantage of BIC is infinite Q and zero line width in the spectrum. However, in practice, BICs are transformed into quasi-BICs of finite Q factor and appear in the form of Fano resonances[50] or electromagnetically induced transparency (EIT)[51] in the spectrum. The physics of BICs can be explained by eigenmode analysis, multipolar decomposition, and group theory. While solving the eigenvalue problem, the modes with real eigenfrequencies and Q-factor > 10^4 are considered. Cartesian multipolar decomposition of selected eigenmodes is carried out to obtain the dominant multipole components. If a mode has a dominant component in the z direction, it implies the absence of far-field radiation in the z-axis, and this mode cannot be excited by a normally incident plane wave of any linear polarization, indicating symmetry-protected BICs[52–54]. In the case of accidental BICs, multipolar moments destructively interfere with each other so that there is no net radiation in a particular direction or certain k wave vector.

Similar to the nuclear physics theory, the concept of anapole mode is extracted and implemented in electromagnetics for gaining light confinement in the resonator[55,56]. The toroidal moment which completes the family of multipoles, exhibits the torus-shaped

current distribution. In 2015, the destructive interference of both an electric dipole and toroidal dipole resonance was studied in the case of the dielectric, which leads to the formation of an anapole state while suppressing the far field[57]. One of the distinctive abilities of the toroidal dipole is that it radiates with the same angular momentum as that of an electric dipole. However, the analysis of the phase difference of interfering electric and toroidal components gives the condition to validate the presence of anapole[58,59].

$$p^{(e,m)}_{i_1\cdots i_n} + \frac{ik_d}{v_d} T^{(e,m)}_{i_1\cdots i_n} = 0 \qquad \ldots (9)$$

Till now, various mathematical concepts and underlying physics of dielectric metasurface have been discussed that may be utilized to create various applications such as beam steering (*i.e.*, deflectors), meta-lensing, meta-holograms, and sensors based on wave front manipulation. Other than these promising applications, metasurfaces are also finding interest in combining two-dimensional materials, nonlinear effects, quantum states preparation, sources, and integration with optical fibers. The following sections provide comprehensive glimpses and an overview of such applications with an outlook.

3. Applications spectrum of all-dielectric metasurfaces

Metasurfaces have been used for various applications due to their ability to replace conventional bulk optical devices. The most significant advantage of the metasurface is its small device footprint, ultra-thin, contrary to the traditional devices available in the market. In this section, progress on metasurface devices for various applications is discussed.

3.1 Wavefront manipulation

Many methods, both numerically and experimentally, are suggested for wave front engineering, where the approach relies on the phase manipulation of the generated light from 0 to 2π. One of the methods is the resonant phase, where the structural parameters of the resonators vary such that a single nanoresonator oscillation provides a phase delay of 0 to π, which can be extended to the full range of 0 to 2π when an array of nanoresonators is considered. Pancharatnam-Berry (PB) phase is based on the geometric phase modification obtained by spatially rotating each nanoresonator in an array[14,16,60,61]. All such phase manipulation techniques can be used for beam steering, meta-lensing, polarization converters, and meta-holograms, as depicted in Fig. 4.

3.1.1 Beam Deflectors

The phase change accumulated along the optical path can be utilized for manipulating the wave front of light. The introduction of subwavelength nanostructures between two media introduces the phase discontinuity at the interface; this abrupt phase change is addressed by the generalized Snell's law[8] as follows,

$$n_t \sin(\theta_t) - n_i \sin(\theta_i) = \frac{\lambda_0}{2\pi}\frac{d\phi}{dx} \qquad \ldots (10)$$

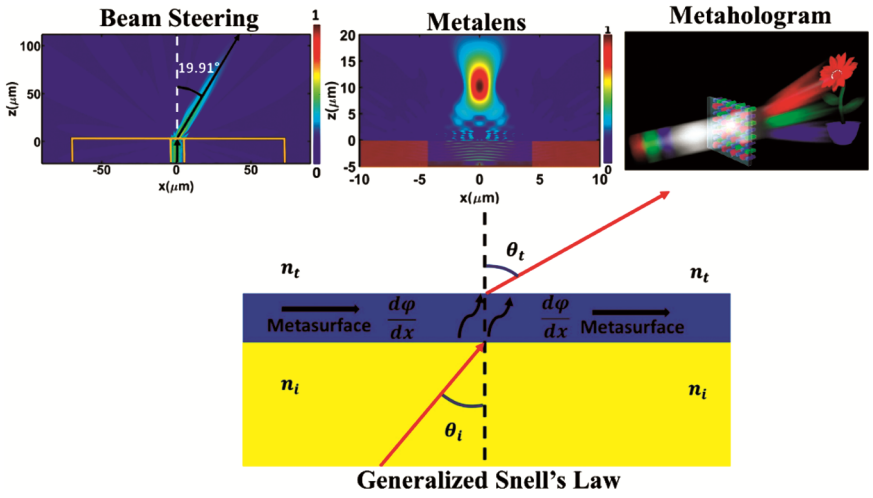

Fig. 4 — Snell's law for refraction (lower panel) where phase discontinuity is introduced by metasurface at the interface of two media. The phase gradient is utilized in applications such as beam steering,metalens[62], and meta-hologram (upper panel). Reproduced with permission[63]. Copyright 2016, American Chemical Society.

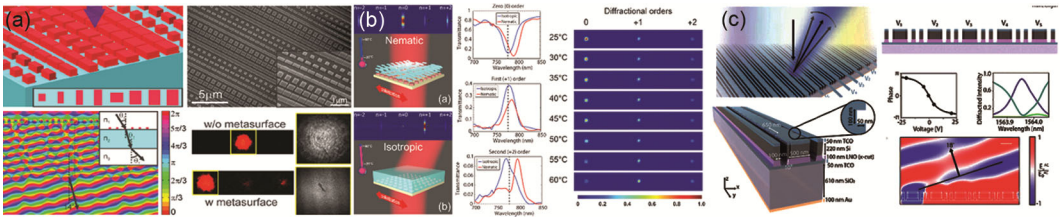

Fig. 5 — (a) Schematic and SEM image of nanoblock metasurface illustrating the beam steering at 14º. Position of beam without and with metasurface along with the photograph of input and output beam is also shown. Reproduced with permission[64]. Copyright 2015, American Chemical Society. (b) Beam deflection and various diffraction orders for two liquid crystal states at different temperatures. Reproduced with permission[73]. Copyright 2018, American Chemical Society. (c) The array of nanobar with nanofins metasurface to achieve beam steering for different bias voltages. The phase gradient 0 to 2π across the supercell with beam deflection of 18º at wavelength 1563.93 nm is depicted. Reproduced with permission[71]. Copyright 2022, American Chemical Society.

where n_i and n_t are the refractive indices of two media, respectively, where θ_i and θ_t are the incidents and refracted angles, the $\frac{d\phi}{dx}$ represents the phase gradient along the interface (Fig. 4). Here, the refracted and the reflected light can have a random trajectory for a constant phase gradient along the interface. The generalized Snell's law was first used for demonstrating wave front shaping and manipulation using V-shaped metallic nanoantennas[8], where the phase change of 2π was obtained by changing the geometrical parameters of the nanoantennas to steer the beam. Due to the ohmic losses and cross-polarization coupling, the metallic subwavelength nanostructures tend to have poor transmission efficiency. The low-loss, high refractive index metasurface based on Huygens' principle is used for high-efficiency beam deflectors[64,65], as shown in Fig. 5(a), which are of resonant type, whereas some beam deflectors can also be of non-resonant nature[66]. Various types of beam steerers have been reported since the generalized Snell's law was proposed. One of them is dielectric membrane metasurface-based beam deflectors that exhibit high transmission efficiency from visible to long wavelength IR due to the absence of substrate, which constrains the metasurface's spectral response[67,68]. The efficiency and the Q-factor of the deflected beam can be enhanced further by employing the BIC concept (Fig. 5(c))[69–71], where the metasurface function is 'local' or 'nonlocal' or through a weak coupling of the incident light to the guided mode resonance (GMR)[72].

When the overall response of a metasurface depends on an individual nanoresonator's characteristics, it is considered as 'local.' In contrast, a 'non-local' response arises due to collective modes of composite metasurfaces (*i.e.*, metasurface formed by the many adjacent nanoresonators), resulting in narrow spectral line width. In the case of a nonlocal metasurface, there is no spatial control over the output wavefront. The advantage of using a nonlocal metasurface over the local metasurface is enhanced light-matter interaction and the ability to detect minor refractive index changes[74,75]. The non-local metasurface based on quasi-BIC is used to develop the thermo-optic and wave front shaping modulator where the wave front is turned on and off due to the wavelength shift in response to the refractive index tuning and mechanical strain. It is also used to develop multifunctionality in the metasurfaces[76]. Generally, beam deflectors are static and can be made dynamic through electrical tunability that is realized using free carrier modulation[77], switching the electro-optical[78,79], thermo-optical[80], electromechanical[81], liquid crystal (Fig.5(b))[73,82], and phase change material[83]. The efficiency of the device can be further improved through various optimization techniques (such as multi-objective level set optimization[84]), machine learning, and artificial intelligence[85].

3.1.2 Meta-lens

Optical lenses are the most important components in bulk optics used to focus light and create images. The conventional lenses are thick, and their focusing mainly relies on the accumulated phase, which poses a challenge in downscaling. Metalens are based on the metasurface and the alternative of traditional lenses. The local phase discontinuity provided by each nanoresonator is used for focusing the light. The first metalens was made up of plasmonic nanoantenna[86], but the overall efficiency was poor due to the large intrinsic losses. Low-loss dielectric metasurfaces are preferred over ohmic losses and improved efficiency, high-quality imaging, and focusing. Lin *et al.*[88]

reported the first dielectric metalens where silicon nanoresonators-based phase gradient was used to create lenses and axicons. The advantages of metalenses over conventional lenses are (i) monochromatic and chromatic aberrations, (ii) multi-functionality and a high degree of freedom for wave front shaping, and (iii) CMOS-compatible due to the use of dielectric material[61,87]. For focusing, the incident light at focal point f, the phase ϕ of the metalens should constructively interfere and satisfy the following equation[86]

$$\phi(x,y)=\frac{2\pi n}{\lambda}\left(f-\sqrt{x^2+y^2+f^2}\right) \qquad (11)$$

where r is the radial distance, f is the focal length, and λ is the wavelength. The finite number of nanostructures are used in designing a metalens that imparts discrete phases instead of continuous phases in the range of 0 to 2π[88]. The difference between the reference spherical wave front and the discretized phase envelope is known as the wave aberration function. The performance of metalens depends on the Strehl ratio (SR), defined as the normalization of peak intensity to that of the Airy disk[61]. The dispersion due to the phase accumulation generally results in large chromatic aberration in diffractive optics. So, to overcome the chromatic aberrations, dispersive phase compensation is done as in ref.[89] or the metalens doublets were designed as in ref[90,91] (Fig. 6(a)). The high-efficiency polarization-insensitive metalens and high SR have been developed for high-resolution imaging in the visible region[92]. It is possible to achieve broadband focusing in achromatic metalens through the phase, group delay, and group delay dispersion engineering or through the geometrical design to control phase and dispersion in the visible region[93–95]. In the ref.[96] multi-wavelength achromatic focusing is demonstrated through a single phase profile. The metalens in the ref.[97] focuses light on the detector after it passes through the substrate resulting in solid immersion-type metalens. This technique is compatible with the back illuminated focal plane arrays. Recent studies have shown that the fabrication of large areas of metalens up to centimeters in diameter is possible through the layout compression algorithm and stepper photolithography in near-infrared[98] and deep ultraviolet stepper lithography invisible region[99]. To obtain large-scale, highly efficient metalens topology optimization is done by combining the individually optimized metasurface to reduce the optimization time or by using an inverse design technique in three dimensions for an a periodic complex meta-atom[100]. Currently, metalenses are developed to realize visible chiral imaging[101], full color cameras[102], single-shot depth sensors[103], full Stokes polarization cameras[104], aberration correction in three dimensions positioning single-shot metalens[105], Jones matrix hologram[106] and generation of multiplexed vortex nanolasers[107].

3.1.3 Meta-holograms

Holography is a complex engineering problem for wave front shaping that finds application in sensors, cryptography, data storage, and so on[108–110]. It is an imaging technique for recording and reconstructing

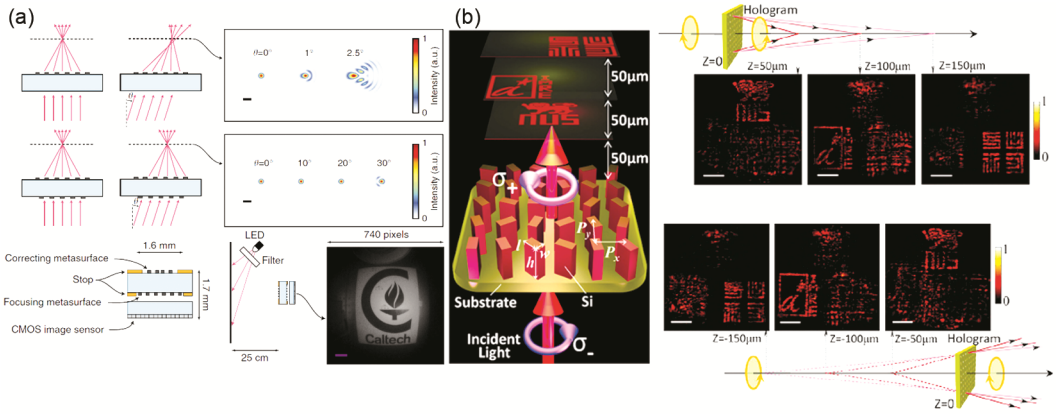

Fig. 6 — (a) Illustration depicting spherical aberration-free on and off-axis focusing of light (left panel) and simulated focal amplitude for different angles by singlet lens. Also, monochromatic aberration correction by a doublet lens is seen. Schematic of miniature camera realized using doublet lens and CMOS image sensor) and imaging setup and captured image by the camera is also shown. Reproduced with permission[91]. Copyright 2016, Nature Publishing Group. (b) Illustration of spin modulated hologram generation, where experimental results of reconstructed holographic image for a left-handed spin and convergent wave front and right-handed spin and divergent wave front. Reproduced with permission[117]. Copyright 2016, Wiley-VCH Verlag GmbH & Co. KGaA, Weinheim.

the intensity and phase of a target wave[111]. Earlier holograms were based on free-space lasers[112]. With the invention of computer-generated holograms, a breakthrough has been achieved in the field of digital holography[113,114]. Typically, traditional holography is limited by large pixel size and space bandwidth that impede real-life applications[115]. With the advancement in the nanofabrication technique, optical elements such as diffractive gratings, metamaterials, and metasurfaces can scale down the bulky macro-scale interference-based generation method to the nanoscale. Among these, all-dielectric metasurfaces have shown great potential in controlling the phase and transmission through well-defined scattering behavior and serve as a good pathway to implement the holography-based design. Three nano-blocks are multiplexed in a subwavelength unit to constitute a meta-molecule for targeting red, blue, and green, where achromatic and highly dispersive meta-holograms with high resolution have been demonstrated[63]. TiO_2 nanofins are designed with absolute efficiency of greater than 78% for red, blue, and green wavelengths and demonstrated through an example by reconstructing the Harvard logo at 480nm, 520nm, 540nm, 600nm, 620nm, and 640nm wavelengths[116]. A novel Si nanostructure-based metasurface employing 8-level of modulation through geometric phase has been reported[117] that manipulates the spin of the light in the visible wavelength, where the metasurface is comprised of position-varying silicon nanorods to exhibit multicolor holography without higher-order diffraction and twin image issue as shown in Fig. 6(b). Holograms in visible regions have been reported so far. However, recently, polarization-insensitive Huygens metasurface in telecommunication wavelength was introduced[118], used to create a hologram of 'hυ' with a transmittance efficiency of 82% and imaging efficiency of 40%. Broadband, high-efficient holograms have beendemonstrated[119] with high polarization sensitivity and chiral imaging functionalities using the concept of detour phase. The hologram operates from the visible to the near-infrared and has efficiency as high as 75% in the 1.0 to 1.4 μm wavelength range by compensating the inherent dispersion of the detour phase with that of the subwavelength structure. Nonlinear holograms were generated using a plasmonic metasurface[120] that usesa high-efficiency cyan and blue third harmonic generation (THG)-based hologram using an all-dielectric C-shaped Si metasurface.

The C-shaped metasurface provides precise control over the fundamental and higher-order resonances such that the fundamental resonance enhances the THG and which is further employed to obtain an overlap with the higher-order resonances for redistribution in the air gap. Due to this, absorption loss decreases at shorter wavelengths and has a high enhancement factor of 230. Multifunctional single layer dielectric metasurface combining two functionalities of color printing and computer generated multiplexed holograms were demonstrated in[121, 122] by modulating spectral and spatial responses at a subwavelength scale. In[121], the Si dimer and nanofins metasurface is illuminated by white light, and the colored image appears while under the red and green light, two different holographic images are projected in the farfield; whereas in[122], dynamic bifunctional metasurface for holography and the color display has been reported, where five meta-holograms are multiplexed for two wavelengths together with the structural color. Also, these holograms can be dynamically switchable by selectively turning "on" and "off." Currently, the field of topological modification of light field is a hotspot for fundamental research. The concept of holographic metasurface based on PB and propagation phase is used to generate two topological configurations, as demonstrated in[123], where the optical vortex and knots are switchable based on the polarization of the incident light. Generally, metasurface based holograms suffer from reconstructed image degradation if it is moved away from the focal plane. To overcome this issue, the meta-axilens phase superimposed with hologram for continuous imaging within a certain range has been proposed[124], which helps in the reconstruction of holograms in different planes simultaneously. On the other hand, the geometric phase enabled novel design strategies to accommodate polarization insensitivity and high bandwidth has been reported[125] due to a trade-off between polarization insensitivity and bandwidth. The metasurface was fabricated using hydrogenated amorphous silicon, and the hologram was reproduced with high image fidelity and efficiency[125].

3.2 All-dielectric biosensors

Biosensors are devices critical for capturing bio-chemical information for detecting and sensing analytes[126,127]. In the past few years, the world has

seen significant advancement in point-of-care diagnostic devices such as blood glucose monitoring[128], rapid antigen detection[129,130], home pregnancy detection, and so on[131]. For the detection of analytes, various techniques have been used where the light is confined in subwavelength nanostructure for enhanced electromagnetic field interaction with the analyte[132]. To date, various metallic nanostructures are used for biosensing applications due to strong electric field enhancement but radiative losses impose limitations[133,134]. To avoid such limitations, dielectric nanostructures came into the picture due to high refractive index contrast and low material losses[135].The sensing parameter while designing a metasurface are working wavelength, field confinement and enhancement, resonance bandwidth and quality factor. Among these, Q factors is the most critical parameter and it is defined as the ratio of the resonant wavelength to the full width half maximum (FWHM).In other words, quality factor can also be quantified in terms of loss. The Q factor is directly related to the field enhancement ($E^2 = \gamma_{rad}(Q^2/V)$, where E is the field enhancement, γ_{rad} is the radiative decay ratio, and V is the mode volume of the nanoresonator)[136]. Narrower the FWHM, higher will be the quality factor and field enhancement. Higher Q factor is desirable in refractometric sensing and spectroscopy[137]. But high Q factor has its own limitations such as in surface-enhanced infrared absorption (SEIRA) and circular dichroism-based spectroscopy where narrow bandwidth cannot cover the large molecular vibrational band of the sensing molecule. So there has to be a trade-off in the Q factor value depending upon the type of sensing and nanoresonator shape and material to achieve best sensing[135]. Sensors are generally graded on account of sensitivity, the figure of merit (FOM), sensor resolution, and limit of detection (LOD)[138]. Sensing could either be refractometric or surface enhanced spectroscopic sensing. In refractometric sensing, the analyte interacts with near field hotspots of the metasurface that leads to a redshift in resonance due to the change in local refractive index which is detected by the resonance, which is quantified by the measurement of sensitivity. Sensitivity is a measure of the shift of the resonant wavelength for a given refractive index variation as follows,

$$S = \frac{\Delta\lambda}{\Delta n} \quad \ldots (12)$$

where $\Delta\lambda$ is the change in wavelength, and Δn is the change in local refractive index. The performance of the sensor is given by FOM, which is defined as the ratio of sensitivity S to that of FWHM of resonant wavelength.

$$FOM = \frac{S}{\text{FWHM}} \quad \ldots (13)$$

The earliest reported all-dielectric metamaterial sensor was in 2014[139], where silicon metasurface made of nanohole arrays was used to detect the refractive index change with the S = 205 nm/RIU and FOM nearly equal to 21. Biotin functionalized Si nanodisk metasurface[140] is used to detect the streptavidin of concentration 0.1 nmol/L through Mie-induced magnetic resonances. Similarly, Si disk, when combined with microfluidic, is used to create a lab-on-chip platform for detecting the Prostate Specific Antigen (PSA) cancer marker with LOD ~ 0.69 ng/mL[141]. The physics of BICs is also employed for making highly sensitive biosensors. Label-free sensing of the monolayer of an ultra-low weight molecule (186Da) using a photonic crystal based metasurface based on the principle of BIC[142] was demonstrated. In another work[143], the concept of BIC was used where mirror symmetry broken elliptical nanoresonators were used for ultrasensitive detection through hyperspectral imaging; the device has bulk sensitivity of 263 nm/RIU. It can detect low molecules of IgG, up to three molecules per μm^2. This sensor is the best example of utilizing an imaging technique for spectrometer-less ultra-sensitive biosensing. Using the similar geometry of elliptical nanoresonators, the sensing of Microcyctin-LR, a toxic pollutant with a LOD of 0.002 µg/L, was reported[144]. In another interesting work[145], the integration of metasurface and microfluidics on an imaging platform for real-time ultrasensitive detection of breast cancer extracellular vesicles has been demonstrated. The device employs quasi-BIC modes in a dimer-type metasurface where mirror symmetry is broken (Fig. 7(a)). It has a LOD of 133 femtomolar while detecting extracellular vesicles. Dielectric metasurface, similar to its metallic counterpart, lacks sufficiently robust response in the visible to trap photons. Using the concept of inverse design for geometrical deformation, one can create material with desired properties such as ultrahigh refractive index in visible region[146]. The deformed geometry supports quasi-BIC resonances and has differential sensitivity

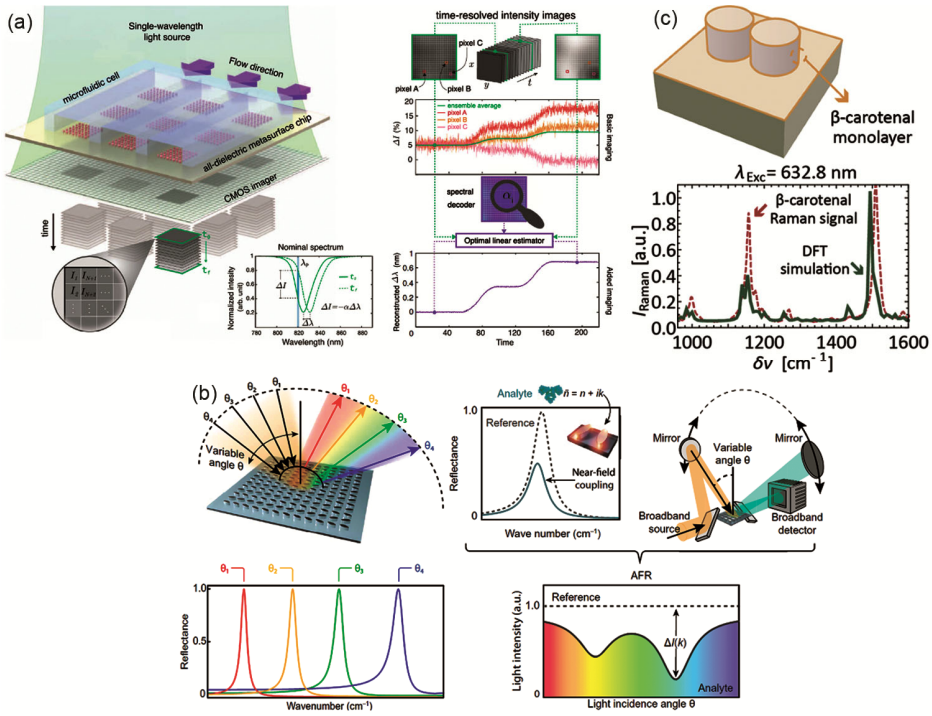

Fig. 7 — (a) Illustration of the two-dimensional array of metasurface integrated with the microfluidic cell with three channels and response captured by the CMOS camera. Introducing biomolecules creates a red shift in resonances (lower panel).Reproduced with permission[145]. Copyright 2021, Springer Nature. (b) Schematic of angle-resolved absorption finger printing. Reproduced with permission[147]. Copyright 2019, American Association for the Advancement of Science. (c) Si dimer for detection of β-carotenal monolayer using SERS. Reproduced with permission[148]. Copyright 2018, American Chemical Society.

of 290 nm μm^{-1} RIU^{-1}. Apart from refractometric sensing, there is vibrational spectroscopic sensing which detects not only molecules but also gives chemical information about such molecules. Both SERS (surface-enhanced Raman spectroscopy) and SEIRA spectroscopy techniques can be realized with metasurface to enhance light-matter interaction for label-free sensing. The former approach monitors the molecular vibrations through inelastic scattering, while the latter technique measures infrared absorption and provides chemical information. Pixelated dielectric metasurface[50] is used for molecular fingerprint detection off surface bound analyte. The device uses the concept of super cavity modes, where the molecular absorption signature at various spectral positions is measured and translated into a barcode for imaging. In another work[147], the Ge based metasurface utilizes the concept of BIC for developing the SEIRAS based sensor to detect absorption molecular fingerprints. Here, the resonance wavelength is tuned by changing the angle of incidence that is correlated to the intensity of infrared absorption for fingerprints of the molecule at the resonant wavelength, as shown in Fig. 7(b). The aforementioned detection techniques do not make use of a spectrometer. In another work present in[148], SERS was implemented to detect a self-assembled monolayer of β-carotenal over Si dimer placed over the sapphire substrate (Fig. 7(c)). In all-dielectric metasurface, field enhancement is still poor as compared to metal-based metasurface, but efforts are made to improve it by optimizing the design of metasurface such that it supports strong near field enhancement outside the volume of a nanoresonator, for example, silicon nitride-based metasurface supporting quasi-BIC resonances provides field enhancement of 10^3 in fluorescence emission and Raman scattering[149], which can be utilized for SERS.

3.3 Integration of optical fiber with all-dielectric metasurfaces

The concept of lab-on-fiber or fiber-metatip is gaining huge interest among the scientific community as a strong field enhancement architecture can be created and fabricated on the optical fiber tip[150]. Significant advancement has been seen in this field, including integrating optical fiber with metasurface for controlling the light-matter interaction at the nanoscale. This paves an alternative route to develop

all fiber-based multifunctional ultra-compact nanoprobes for applications such as sensing, imaging, lensing, optical fiber tweezer and so on. It also enhances the practical applicability of metasurface in practical scenarios as it becomes much easier to couple light in and out from an optical fiber. One of the earliest applications of lab-on-fiber was the SERS. The array of metallic nanoantennas was fabricated at the optical fiber facet, while the other end was used for input and detection purposes[151,152]. Generally, nanoantennas are fabricated using the FIB milling technique, but due to inadvertently gallium ion tube into silica and gold, the response of the array might alter. To avoid this, nanostructures are first made by electron beam lithography onto a silicon substrate, stripped off from the silicon surface, and transferred onto the fiber tip. This method is known as decal transfer[151]. Other methods used for creating fiber tips are nanoimprint lithography[153] and interference lithography[152] for high throughput fabrication. Quasi-one-dimensional Bessel beam have also been generated[154] by patterning the slit-metallic groove structure on the fiber tip to form a plasmonic lens. Such a patterned fiber tip generates a Bessel beam of 0.8 μm at a 2 μm focal length.

The hybrid-metal dielectric nanostructures were also made onto optical fiber tip that support LSPR for refractive index-based sensing and detection of acoustic waves[155]. In 2017, the first experimental demonstration of generalized Snell's law for beam steering and its usage as a sensor was carried out as a proof-of-concept on fiber meta tip. The phase gradient was created using a plasmonic nanohole array at the interface of the optical fiber tip and air[156]. When Bragg grating in thin Si film is fabricated onto the fiber tip, it exhibits a quality factor (Q > 300) resonance through the FIB milling technique, which was then used for dispersion compensation due toits highly dispersive nature[157]. Fiber metatipis also used in applications such as polarization conversion and polarizing beam splitter to replace the bulk optic for obtaining ultra-compact and low-loss devices. A polarization converter has also been made of silicon cylindroid dielectric metasurface on the optical fiber[158]. Also, the linear polarization state is rotated to obtain radial or azimuthal polarization mode. For manipulation of the optical beam, a polarizing beam splitter is directly fabricated on to fiber tip using a direct laser writing technique[158]. Highly efficient two-dimensional beam steering and meta-lensing using the TiO_2 nanocylinder based metasurface implanted over the single-mode fiber has been presented[62], as shown in Fig. 8.

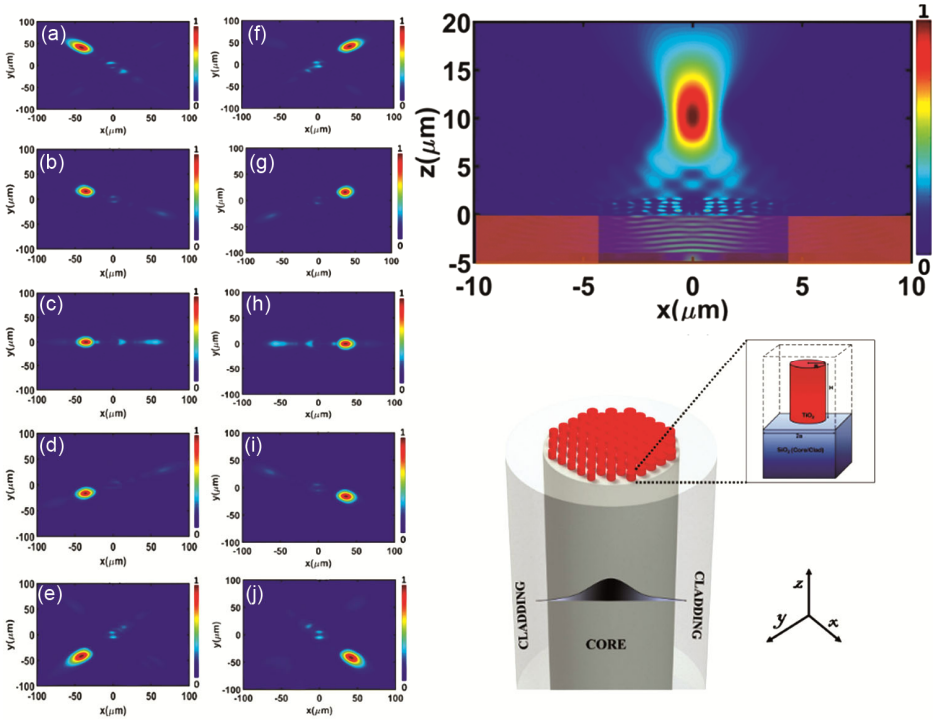

Fig. 8 — Schematic of fiber metatip and unit cell of nanocylinder. Two-dimensional beam steering is shown as normalized E_y in the transverse plane. Meta-lensing as seen in the cross-sectional plane[62].

3.4 Integration of two-dimensional materials with all-dielectric metasurfaces

Thinning of bulk crystals down to a few or single layers gives rise to two-dimensional (2D) materials, bonded in-plane by a strong covalent bond and out-of-plane by weak vander Waals forces, rendering remarkable electrical, optical, and mechanical properties[159]. Some of these include indirect to direct bandgap transition, enhanced electrical and thermal conductivity, extremely confined subwavelength modes, and tunable response, to name a few, which can be exploited for various future applications such as polarizers, single photon sources, sensors, lasers, perfect absorbers and photodetectors and so on[160–166]. 2D materials support quasiparticles — half-matter, half-light states, formed by the strong coupling of either free space photon with free electrons in metals — Plasmon Polaritons (PPs)[167], or photons coupled with lattice vibration of polar crystals — Phonon Polaritons (PhPs)[168]. Another type of quasiparticles are excitons (tightly bound electron-hole pair),which originate due to the absorption of an incident photon in semiconducting materials[169]. Graphene, the eldest 2D material, consists of carbon atoms arranged in a hexagonal honeycomb lattice. It is a zero bandgap semimetal offering exceptional thermal and optical conductivity, which can be tuned by doping, voltage, and temperature[170]. The unprecedented and exceptional properties of graphene make it the most widely studied 2D material, which has sparked a quest to explore a two-dimensional variant of existing bulk materials. Hexagonal boron nitride (hBN) behaves as an insulator with the band gap of 6eV and is often used as the substrate for graphene[171]. Another genre of 2D materials is Transition metal dichalcogenides (TMDCs). Each individual layer of TMDCs consists of three atoms (MX_2 or X-M-X here, M and X is transition metal and chalcogen atom, respectively) bonded in trigonal prismatic configuration by strong covalent bonds. Mostly studied TMDCs are formed by transition metals such as Molybdenum and Tungsten in conjugation with group-VI elements of the periodic table (Sulfur (S), Selenium (Se) and Tellurium (Te)) as chalcogenides[172]. They exhibit layer dependent band gap transition from indirect to direct, with its band gap lying in visible and near-infrared ranges (1.0-2.1 eV)[173–175]. Two-dimensional TMDCs support exciton (bright and dark) with high binding energy ranging from 0.2eV in case of Molybdenum Sulfide (MoS_2) to 0.55eV for Molybdenum selenide ($MoSe_2$)[176]. These values are quite high with respect to conventional quantum wells and allow room temperature operation. Spin-orbital coupling and breaking of inversion symmetry in 2D TMDCs provide chiral effects to incident light. Excitonic transitions at room temperature, direct bandgap, and chiral electronic states make TMDCs an ideal candidate for valleytronics, photonics, and optoelectronic applications[177]. However, atom thick 2D materials limit the performance of 2D materials based photonic devices due to weak light-matter interaction. One of the most promising solutions to improve light-matter interaction is a hybrid approach that integrates 2D materials with resonant nanostructures. Although several studies have been devoted to plasmonic 2D material hybrid structures, high dissipative ohmic losses of metals in visible and near-infrared (NIR) wavelength range limits their use to low frequencies only[178]. Dielectric metasurfaces of high-index materials have successfully replaced metals with low-loss and improved response in terms of high-Q factor and enhanced mode volume, allowing significant light-matter interaction[179]. The marriage between 2D materials and dielectric metasurfaces allows one to bear fruits with the characteristics of both constituents.

For example, Graphene can absorb only 2.3% of incident light[180] and cannot provide sufficient interaction with light for various graphene based devices[181–183]. Strong light- matter interaction has been achieved by patterning graphene in nanoribbons[184] or placing the graphene layer nearnanostructures that support high electric field confinement[184]. Graphene can exhibit plasmonic response across the mid-infrared and terahertz spectral ranges only; patterning of graphene cannot enhance light-matter interaction in the visible and near-infrared range. To resolve the above-mentioned issue, hybrid configurations in which 2D materials are integrated with dielectric nanoresonators are evolved that provide flexible control of bandwidth, adsorption efficiency, and resonant wavelengths. In an early report, the periodic structure of a silicon nanodisk with a graphene layer is proposed by Wang *et al.*[185]. The designed metasurface supports MD dominated quasi-BIC, and when the radiative rate of dipole mode is equivalent to the dissipative loss of graphene, critical coupling between the metasurface and graphene results in maximum absorption of graphene, as shown in Fig. 9(a). Also, modulation in absorption

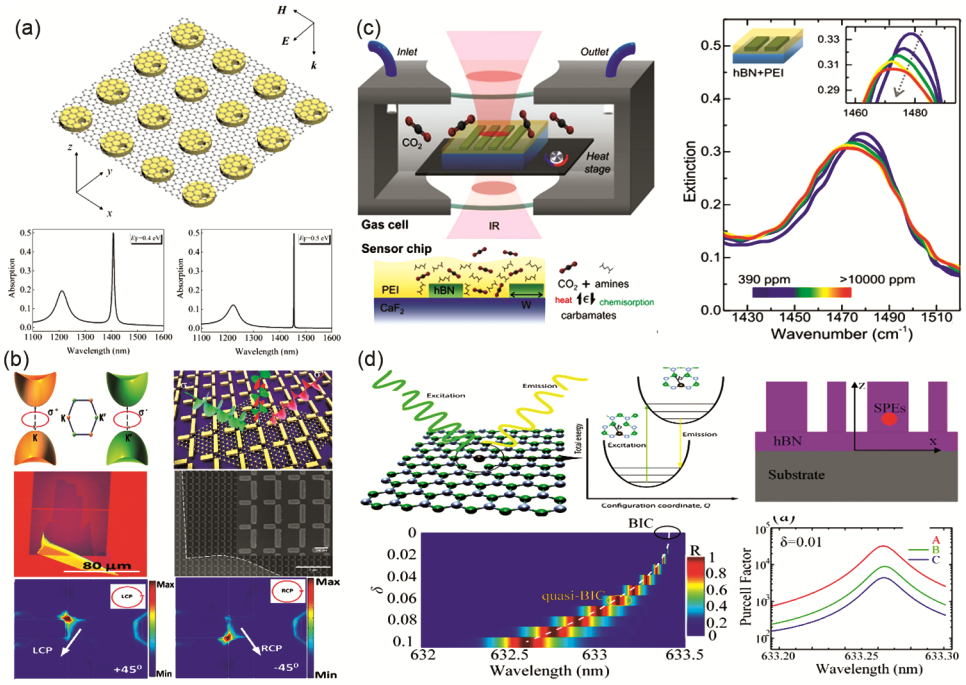

Fig. 9 — Integration of all-dielectric metasurfaces with two-dimensional materials. (a) schematic of silicon nanodisk metasurface with monolayer graphene and absorption spectra at critical coupling for different Fermi potentials of graphene, reproduced with permission[185]. Copyright 2020, IOP Physical Review B. (b) schematic representing valley polarization in TMDCs monolayers onchiral metasurface; optical images and simulated electric field in hybrid structure for incident linear polarization are also shown, reproduced with permission[212]. Copyright 2019, Optical Materials Express. (c) IR gas sensing setup using sensors chip which consists of hBN+PEI nanoribbons; measured extinction spectra for various concentrations of CO_2 (expressed in parts per million), reproduced with permission[213]. Copyright 2021, ACS Photonics. (d) schematic of photon emission from defect mediated photoluminescence process in hBN; hBN grating supporting BICs for enhancement of single photon source placed inside hBN metasurface. Simulated reflection spectra of hBN MS for various asymmetry parameters (δ) with respect to wavelength and enhanced Purcell factor are also exhibited. Reproduced with permission[214]. Copyright 2021, IOP Publishing.

wavelength and peak intensity is attained with the varying Fermi level, number of graphene layers, and structural parameters. In[186], the graphene monolayer is sandwiched between a silicon photonic slab and substrate, working in a critically coupled regime to achieve highly efficient light absorption alongwith increased bandwidth of peak absorptivity. In another report[187], silicon nanograting with graphene working in an over-coupled regime for the NIR range is proposed, which supports symmetry-protected quasi-BIC states. Highly efficient absorption of graphene is achieved due to enhanced light-matter interaction facilitated by the formation of hybrid TD-EQ modes. The absorption amplitude and resonant wavelength can be tuned by varying incidence angles and the Fermi potential of graphene. Near perfect absorption of graphene is also recently reported with the introduction of symmetry-protected BICs in amorphous silicon nanocuboids[188]. Thereafter, various studies have been conducted in metasurface design, structural parameters, and various ways to achieve strong coupling between 2D materials and metasurfaces for various applications such as refractive index-based sensors, mid-infrared spectroscopic fingerprinting, perfect absorbers, shaping and enhancing directional emission, active wavefront shaping, detection of molecules based on their chiral response and adding tunability to passive structures.

One of the most appreciated applications of metamaterials is sensing, as they support highly confined electromagnetic fields, popularly known as hotspots. However, ohmic losses in traditional metals hamper their performance. The high FOM, no ohmic losses of dielectric metasurfaces, and additional modes such as magnetic modes (not supported in metallic metamaterials) provide better confined response (highly desired for sensing and spectroscopic applications). A further enhancement is achieved by integrating 2D materials with metasurfaces[189,190]. Two-dimensional materials with high surface-to-volume ratio and on-surface dangling

bonds provide additional binding sites to analytes, enhancing detection. Fano resonance in silicon nanorods separated with a nanogap on SiO_2 substrate has been used for refractive index-based sensing[191].

Additionally, the presence of graphene improved FOM and sensitivity of 956 RIU^{-1} and 430 nm/RIU, respectively. In another report[192], silicon nanocubes coupled with hollow silicon on a quartz substrate decorated with a graphene monolayer are designed. The proposed structure exhibits high-Q EIT with peaks as high as 97.5%, aided by the coupling of one bright mode (supported by silicon nanocube) and dark mode (supported by hollow nanocube). In[193], the authors proposed high-Q Fano resonance in asymmetric silicon disks with enhanced light-matter interaction. The biosensor is proposed for hemoglobin sensing with aFOM greater than 378 RIU^{-1} and sensitivity as high as 550 nm/RIU. The high sensitivity for the surrounding environment and dynamic tunability of EIT by varying the Fermi potential of graphene allows its application as a highly sensitive sensor and switch in the NIR range. Other similar works with metasurface/graphene/substrate configuration for EIT modulation and high-Q sensors with varying geometry of nanostructures are reported in[193–198].

In TMDCs, spin-forbidden dark excitons cannot decay radiatively due to their transition in an in-plane dipole-forbidden direction and, thus, not possible to detect in photoluminescence (PL) measurements[199]. One of the simple approaches to visualize them is to allow efficient coupling of dark excitons to resonant nanostructures, where the excitonic emission couples to out-of-plane modes supported by nanostructure and can be emitted directively[200,201]. Additionally, to shape or enhance emission from 2D materials, the incorporation of nanostructures supporting a high front-to-back scattering ratio and high-Q can provide directional emission with enhanced quantum efficiency. An enhancement in the directional scattering of PL from 2D-MoS_2 is observed[202] by placing a silicon nanowire on its surface. Further etching the underneath layer of 2D-MoS_2 using Si nanowire as a mask increased the front-to-back ratio of far-field. In another report[203], a similar response of enhanced PL spectra by suspending single layer (1L) 2D-MoS_2 on silicon nanocylinders arranged in a square array pattern. The size of nanocylinders is varied to cover the whole emission wavelength band of 1L-MoS_2 with improved directivity highly desired for low NA collection. Another approach works on attaining strong coupling of emitters placed between nanoresonators and substrate. Such a particle-on-film combination is a well-known geometry for exploring enhanced interaction, as discussed in[204], where a hybrid system for manipulating emission from 1L-TMDCs has been investigated. The hybrid structure contains one layer of different TMDCs on the SiO_2 substrate decorated with silicon nanoparticles (NPs). Magnetic quadruple mode with an electric field confined in a tangential direction further aids the overall directional response of emission. The core-shell[205] configuration, consisting of silicon NPs as the core and 1L-WS_2 as the shell, has achieved strong coupling with Rabi splitting of 116 meV. The splitting could be further enhanced when the surrounding medium is replaced with water.

Patterning of 2D materials into nanostructures to support high-Q modes has recently emerged to achieve strong interaction of geometry confined modes with material supported excitons. The fact that TMDCs have a high refractive index in the visible to NIR range allows their use for high-Q resonant structures[206]. With this view, Verre *et al.*[207] proposed nanodisks of WS_2 supporting structural tunable Mie resonances from visible to NIR range. A large Rabi splitting of 253 meVhas been reported for WS_2 grating on SiO_2 substrate[208], where a slight gap variation producesa strong coupling between the supported quasi-BIC and exciton. In another report[209], perfect reflection from MoS_2 nanoribbons on silica/silicon substrate is theoretically obtained with extremely narrow linewidth and ultrahigh-Q in the NIR range. The resonance wavelength exhibited layer dependent tunable response. Another interesting field of TMDCs photonics is nonlinearity, out of which many exciting phenomena, such as higher-order harmonic generation, holography, and optical beam generation, can be realized. Patterning of 1L-MoS_2 and 1L-WS_2 into nanostructures supporting nonlinear response have been recently reported for vortex beam generation and complex holographic patterns, respectively[210,211]. Boosting and controlling the valley-specific chiral emission is yet another subject of research that primarily concentrates on valleytronic applications, and it has lately gained a significant amount of scientific interest. Unlike metals, dielectric structures can store all the intermediate chiral values of TMDCs and thus are better suited for applications involving the valley degree of freedom of

Fig. 10 — Overview of the applications of all-dielectric metasurfaces in various fields.

TMDCs[212,215]. Chiral metasurface made up of germanium has been integrated with 2D TMDCs[212] to achieve circularly polarized light when linearly polarized is incident (see. Fig. 9(b)). Polar crystals like hBN, Molybdenum Trioxide, and Silicon carbide support phonon polaritons in the mid-infrared range[216]. The PhPs are high-momentum (high-K) modes having characteristics of deeply confined modes, longer propagation lengths, and low-loss when compared to their plasmonic counterparts, *i.e.,* plasmon polaritons. Applications of PhPs include vibrational fingerprinting, detection of trace amounts of analytes through SEIRA and SERS, imaging and single photon sources. However, high-K cannot be directly excited by free-space photons due to momentum mismatch. Nanostructures can fulfill momentum matching criteria enabling the excitation of PhPs. In[213], the carbon dioxide sensor is designed from nanoribbons of hBN on a transparent substrate. Patterning of hBN into nanoribbons allowed momentum matching and, thus, generation PhPs with a high signal-to-noise ratio (refer to Fig. 9(c)). Recently, hBN is patterned on a glass substrate supporting high-Q quasi-BICs in the visible region and produced enhanced emission of single photon emitters in hBN[214], as shown in Fig. 9(d).The concept of a hybrid system consisting of 2D materials and all-dielectric metasurfaces can be a new approach towards various applications in the fields of photonics and optoelectronics. Resonant dielectric metasurfaces supporting high-Q modes, along with a tightly confined electromagnetic field, can further enhance the performance of hybrid structure-based devices. The inclusion of 2D materials can provide additional benefits of active manipulation, benefitting both 2D materials and dielectric metasurfaces. The properties of some 2D materials are intrinsic to their crystal structure and thus cannot be altered. One approach includes forming van der Waals heterostructure so that the materials in the vicinity couple to produce an actively tunable hybridized response[217]. Therefore, stacking various 2D materials to form van der Waals heterostructure combined with other metasurfaces can be a viable option for harnessing the individual properties of each participating material.

4 Conclusions and Outlook

The metasurface is a growing scientific field with a multi-billion market within the next decade due to its unique ability to manipulate and control light at the nanoscale. This review provides a comprehensive overview of all-dielectric metasurfaces with underlying physics and a suitable mathematical framework. Also, various applications of past years, such as wavefront manipulation, biosensors, and integration with optical fiber and 2D materials, have been discussed. Other than this, metasurface has a future prospect in the areas of nonlinear optics, quantum technology, the energy sector, the agro-food industry, biomedical, and more. Fig. 10 provides a perspective and usage of dielectric metasurface in various sectors. Due to the unprecedented control over the incident light, metasurface has shown the pathway to generate and control the nonlinear waves.

Also, it does not require the phase-matching conditions to exhibit nonlinear effects such as second-order nonlinearity (second harmonic generation, sum frequency generation) and third-order nonlinearity (four-wave mixing, third harmonic generation). Some metasurfaces can create new wavelengths through higher harmonic generation from mid-infrared to visible. The efficiency of nonlinear effects can further be enhanced through Fano resonance and BICs. The governing factors that induce a nonlinear optical response in metasurfaces are the frequency and the spatial dispersion that vary from bulk to nanomaterials[218]. By using the engineered subwavelength structures, it is possible to realize nonlinear diffraction[219], holograms[120], nonreciprocal transmission[220], asymmetric parametric generation[221], and many more.

Metasurface also holds promise in implementing quantum vacuum engineering for long-distance information processing[222]. The theory of weakness of the system where measurements are taken after giving some tiny change was proposed in 1988[223]. With the use of dielectric metasurface, this theory helps monitor the precise measurements of the nature of the light beam[224]. The idea of entangled photons over a long distance using dielectrics is found to be significant for achieving high transmission rates[225]. The on-chip integration of entangled qubits[226] and entangled single photons provide information on OAM and spin angular momentum using metamaterial[227]; quantum computing and the possibility of single photon detection at room temperature are the recent areas where metasurface can be used. Metaphotonics has paved the way to use the theory of quantum optics with applications like imaging, sensing, and cryptography[228–231]. Metasurface can also be employed in spin-controlled nanophotonics, where photonic spin-orbit interactions are studied in the photonic spin hall effect. Here the coupling between the spin and orbital degrees of freedom of photons is studied. Prospective future applications of metasurface are not limited to the aforementioned field, but they can also be used in the energy sector for smart windows for radiative cooling, as perfect mirrors, and in the agro-food sector for seed, food, and soil quality checks.

Acknowledgments

The author (SKV)likes to acknowledge the support received from projects, vide no. DST/NM/NT/2018/9(G), IIT/KCSTC/Chair./ NEW/P/17-18/02, and Indian Institute of Technology Kharagpur.

References

1 Wriedt T, *Springer Ser Opt Sci*, 169 (2012) 53.
2 Smith D R, Padilla W J, Vier D C, Nemat-Nasser S C & Schultz S, *Phys Rev Lett*, 84 (2000) 4184.
3 Lu D & Liu Z, *Nat Commun*, 3 (2012)1205.
4 Cumming D R S, Kenney M, Grant J, Escorcia-Carranza I & Shah Y D, *Opt Express,* 26 (2018) 10408.
5 Seddon N & Bearpark T, *Science*, 302 (2003)1537.
6 Chen H, Wu B I, Zhang B & Kong J A, *Phys Rev Lett*, 99 (2007) 063903
7 Landy N I, Sajuyigbe S, Mock J J, Smith D R & Padilla W J, *Phys Rev Lett*, 100 (2008) 1.
8 Yu N, *et al.*, *Science*, 334 (2011) 333.
9 Lapine M, Shadrivov I V & Kivshar Y S, *Rev Mod Phys*, 86 (2014) 1093.
10 Holloway C L, Kuester E F, Gordon J A, O'Hara J, Booth J & Smith D R, *IEEE Antennas Propag Mag*, 54 (2012) 10.
11 Chen H T, Taylor A J & Yu N, *Rep Prog Phys*, 79 (2016) 076401.
12 Hsiao H H, Chu C H & Tsai D P, *Small Methods*, 1 (2017) 1.
13 Decker M & Staude I, *J Opt*, 18 (2016) 103001.
14 Liu W, Li Z, Cheng H & Chen S, *Science*, 23 (2020) 101868.
15 Zhang L, Mei S, Huang K & Qiu C W, *Adv Opt Mater*, 4 (2016) 818.
16 Chen S, Li Z, Zhang Y, Cheng H & Tian J, *Adv Opt Mater*, 6 (2018) 1.
17 Bancroft W D & Gurchot C, *J Phys Chem*, 36 (2002) 2575.
18 Bohren C F & Huffman D R, *Absorption and Scattering of Light by Small Particles*. Wiley, 1998.
19 Tzarouchis D & Sihvola A, *Appl Sci*, 8 (2018) 184.
20 Cantrell C D, *Numerical Methods for the Accurate Calculation of Spherical Bessel Functions and the Location of Mie Resonances*, 2 (1988) 2003.
21 Sudiarta I W & Chýlek P, *Appl Opt*, 41 18 (2002) 3545.
22 Chew H, McNulty P J & Kerker M, *Phys Rev A*, 13 (1976) 396.
23 Kerker M, Wang D-S & Chew H, *Appl Opt*, 19 (1980) 4159.
24 Kerker M, Wang D S & Giles C L, *J Opt Soc Am*, 73 (1983) 765.
25 Pors A, Andersen S K H & Bozhevolnyi S I, *Opt Express*, 23 (2015) 28808.
26 Reena, Kalra Y, Kumar A & Sinha R K, *J Appl Phys*, 119 (2016) 243102.
27 Jiang L *et al.*, *Microw Opt Technol Lett*, 62 (2020) 2405.
28 Shamkhi H K, *et al*, *Phys Rev Lett*, 122 (2019) 193905.
29 Born M, Wolf E & Hecht E, *Phys Today*, 53 (2000) 77.
30 Decker M, *et al.*, *Adv Opt Mater*, 3 (2015) 813.
31 Pfeiffer C & Grbic A, *Phys Rev Lett*, 110 (2013) 1.
32 Bag A, Neugebauer M, Woźniak P, Leuchs G & Banzer P, *Phys Rev Lett*, 121 (2018) 1.
33 Alaee R, Safari A, Sandoghdar V & Boyd R W, *Phys Rev Res*, 2 (2020) 043409.
34 Moreno F, González F, García-Cámara B & Saiz J M, *J Opt Soc Am A,* 25 (2008) 2875.
35 Yang Y, *et al.*, *Phys Rev B*, 95 (2017) 165426.
36 Colegrave R K & Abdalla M S, *Taylor Fr*, 28 (1981) 495.
37 Rakhmanov M, Savage R L, Reitze D H & Tanner D B, *Phys Lett Sect A Gen At Solid State Phys*, 305 (2002) 239.
38 Huang C P & Chan C T, *EPJ Appl Metamater*, 1 (2014) 2.
39 Landreman P E, Chalabi H, Park J & Brongersma M L, *Opt Express*, 24 (2016) 29760.

40 Gromyko D A, *et al.*, *Phys Rev Appl*, 17 (2022) 024015.
41 Friedrich H & Wintgen D, *Phys Rev A*, 32 (1985) 3231.
42 Hsu C W, Zhen B, Stone A D, Joannopoulos J D & Soljacic M, *Nat Rev Mater*, 1 (2016) 48.
43 Marinica D C, Borisov A G & Shabanov S V, *Phys Rev Lett*, 100 (2008) 1.
44 Plotnik Y, *et al.*, *Phys Rev Lett*, 107 (2011) 28.
45 Kodigala A, Lepetit T, Gu Q, Bahari B, Fainman Y & Kanté B, *Nature*, 541 (2017) 196.
46 Fedotov V A, Rose M, Prosvirnin S L, Papasimakis N & Zheludev N I, *Phys Rev Lett*, 99 (2007) 5.
47 Pichugin K N & Sadreev A F, *J Opt Soc Am B*, 32 (2015) 1630.
48 Sharma S, Lahiri B & Varshney S K, *Optics Info Base Conference Papers*, 2022.
49 Hsu C W, *et al.*, *Nature*, 499 (2013) 188.
50 Tittl A *et al.*, *Science*, 360 (2018) 1105.
51 Abujetas D R, Barreda Á, Moreno F, Litman A, Geffrin J M & Sánchez-Gil J A, *Laser Photonics Rev*, 15 (2021) 1.
52 Sadrieva Z, Frizyuk K, Petrov M, Kivshar Y & Bogdanov A, *Phys Rev B*, 100 (2019) 115303.
53 He Y, Guo G, Feng T, Xu Y & Miroshnichenko A E, *Phys Rev B*, 98 (2018) 161112.
54 Sharma S, Lahiri B & Varshney S, *J Phys D Appl Phys*, 56 (2023) 055104.
55 Haxton W C, Liu C P & Ramsey-Musolf M J, *Phys Rev C - Nucl Phys*, 65 (2002) 30.
56 Savinov V, Papasimakis N, Tsai D P & Zheludev N I, *Commun Phys*, 2 (2019) 69.
57 Miroshnichenko A E, *et al.*, *Nat Commun*, 6 (2015) 1.
58 Gurvitz E A, Ladutenko K S, Dergachev P A, Evlyukhin A B, Miroshnichenko A E, & Shalin A S, *Laser Photon Rev*, 13 (2019) 1800266.
59 Pradhan M, Sharma S, Bhaktha S B N & Varshney S K, Higher-Order Anapole in Slanted Nanodisk Resonator, in *Optics Info Base Conf*, (2022) 25.
60 Hasman E, Kleiner V, Biener G & A Niv, *Appl Phys Lett*, 82 (2003) 328.
61 M Pan, *et al.*, *Light Sci Appl*, 11 (2022) 195.
62 Sinha R K, Sharma S, Bag S, Kar S, B Lahiri & Varshney S K, *Opt Laser Technol*, 148 (2022) 107694 .
63 Wang B, *et al.*, *Nano Lett*, 16 (2016) 5235.
64 Shalaev M I, Sun J, Tsukernik A, Pandey A, Nikolskiy K & Litchinitser N M, *Nano Lett*, 15 (2015) 6261.
65 Yu Y F, Zhu A Y, Paniagua-Domínguez R, Fu Y H, Luk'yanchuk B & Kuznetsov A I, *Laser Photonics Rev*, 9 (2015) 412.
66 Su X, Li G, Yang H, Zhao Z, Yu F & Chen X, *J Phys D Appl Phys*, 50 (2017) 345102.
67 Ong J R, Chu H S, Chen V H, Zhu A Y & Genevet P, *Opt Lett*, 42 (2017) 2639.
68 Yang Q, *et al.*, *Adv Funct Mater*, 30 (2020) 1.
69 Contractor R, *et al.*, *Front Opt - Proc Front Opt+Laser Sci*, (2019).
doi: 10.1364/FIO.2019.JTu3A.113.
70 Barton D, Lawrence M & Dionne J, *Appl Phys Lett*, 118 (2021) 071104.
71 Klopfer E, Dagli S, Barton D, Lawrence M & Dionne J A, *Nano Lett*, 22 (2022) 1703.
72 Lawrence M, *et al.*, *Nat Nanotechnol*, 15 (2020) 956.
73 Komar A, *et al.*, *ACS Photon*, 5 (2018) 1742.
74 Kwon H, Sounas D, Cordaro A, Polman A & Alù A, *Phys Rev Lett*, 121 (2018) 173004.
75 Malek S C, Overvig A C, Alù A & Yu N, *Light Sci Appl*, 11 (2022) 905.
76 Malek S C, Overvig A C, Shrestha S & Yu N, *Nanophotonics*, 10 (2020) 655.
77 Salary M M, Farazi S & Mosallaei H, *Adv Opt Mater*, 7 (2019) 1.
78 Holsteen A L, Cihan A F & Brongersma M L, *Science*, 365 (2019) 257.
79 Wu P C, *et al.*, *Nat Commun*, 10 (2019) 1.
80 Rocco D, *Opt Info Base Conf*, 29 (2021) 37128.
81 Kwon H, Zheng T & Faraon A, *Nano Lett*, 21 (2021) 2817.
82 Zou C, *et al.*, *ACS Photon*, 8 (2021) 1775.
83 He J, Shi Z, Ye S, Li M & Dong J, *Opt Express*, 30 (2022) 34809.
84 Dong L, *et al*, *Opt Mater Express*, 12 (2022) 3667.
85 Li Z, Pestourie R, Lin Z, Johnson S G & Capasso F, *ACS Photon*, 9 (2022) 2178.
86 Aieta F, *et al.*, *Nano Lett*, 12 (2012) 4932.
87 Engelberg J & Levy U, *Nat Commun*, 11 (2020) 9.
88 Aieta F, Genevet P, Kats M & Capasso F, *Opt Express*, 21 (2013) 31530.
89 Aieta F, Kats M A, Genevet P & Capasso F, *Science*, 347 (2015) 1342.
90 Groever B, Chen W T & Capasso F, *Nano Lett*, 17 (2017) 4902.
91 Arbabi A, Arbabi E, Kamali S M, Horie Y, Han S & Faraon A, *Nat Commun*, 7 (2016) 1.
92 Khorasaninejad M, *et al.*, *Nano Lett*, 16 (2016) 7229.
93 Khorasaninejad M, *et al.*, *Nano Lett*, 17 (2017) 1819.
94 Chen W T, *et al.*, *Nat Nanotechnol*, 13 (2018) 220.
95 Chen W T, Zhu A Y, Sisler J, Bharwani Z & Capasso F, *Nat Commun*, 10 (2019) 1.
96 Shi Z, *et al.*, *Nano Lett*, 18 (2018) 2420.
97 Zhang S, *et al.*, *Appl Phys Lett*, 113 (2018) 111104.
98 She A, Zhang S, Shian S, Clarke D R & Capasso F, *Opt Express*, 26 (2018) 1573
99 Park J S, *et al.*, *Nano Lett*, 19 (2019) 8673.
100 Li Z, Pestourie R, Park J S, Huang Y W, Johnson S G & Capasso F, *Nat Commun*, 13 (2022) 1.
101 Khorasaninejad M, *et al.*, *Nano Lett*, 16 (2016) 4595.
102 Lin R J, *et al.*, *Nat Nanotechnol*, 14 (2019) 227.
103 Guo Q, *et al.*, *Proc Natl Acad Sci U S A*, 116 (2019) 22959.
104 Rubin N A, Aversa G D, Chevalier P, Shi Z, Chen W T & Capasso F, *Science,* 365 (2019) 1839.
105 Liu W, *et al.*, *Optica*, 7 (2020) 1706.
106 Rubin N A, Zaidi A, Dorrah A H, Shi Z & Capasso F, *Sci Adv*, 7 (2021) 7488.
107 Zhang H, *et al.*, *Adv Mater*, 34 (2022) 1.
108 Kim I, *et al.*, *Sci Adv*, 7 (2021) 15.
109 Guo X, *et al.*, *Nat Commun* 13 (2022) 1.
110 Hesselink L, Orlov S S & Bashaw M C, *Proc IEEE*, 92 (2004) 1231.
111 Hariharan P, *Optical holography : principles, techniques, and applications*, 2nd Edn, Cambridge University Press, 1996.
112 Upatnieks J & Leith E N, *J Soc Am,* 52 (1962) 1123.
113 Lohmann A W & Brown B R, *Appl Opt*, 5 (1966) 967.
114 Matsushima K, *Introduction to Computer Holography*, Cham: Springer International Publishing, 2020.

115 Huang L, Zhang S & Zentgraf T, *Nanophotonics*, 7 (2018) 1169.
116 Devlin R C, Khorasaninejad M, Chen W T, Oh J & Capasso F, *Proc Natl Acad Sci U S A*, 113 (2016) 10473.
117 Huang K, *et al.*, *Laser Photon Rev*, 10 (2016) 500.
118 Chong K E, *et al.*, *ACS Photon*, 3(2016) 514.
119 Khorasaninejad M, Ambrosio A, Kanhaiya P & Capasso F, *Sci Adv*, 2 (2016) 1.
120 Gao Y, Fan Y, Wang Y, Yang W, Song Q & Xiao S, *Nano Lett*, 18 (2018) 8054.
121 Wei Q, *et al.*, *Nano Lett*, 19 (2019) 8964.
122 Yang W, *et al.*, *Adv Mater*, 33 (2021) 1.
123 Guo X, *et al.*, *Laser Photon Rev*, 14 (2020) 1900366.
124 Shen C, Xu R, Sun J, Wang Z & Wei S, *IEEE Photon J*, 13 (202)1.
125 Javed I, *et al.*, *ACS Appl Mater Interfaces*, 14 (2022) 36019.
126 Borisov S M & Wolfbeis O S, *Chem Rev*, 108 (2008) 423.
127 Chen C & Wang J, *Analyst*, 145 (2020) 1605.
128 Peng Z, *et al.*, *J Innov Opt Health Sci*, 15 (2022) 1.
129 Cohen J F, Bertille N, Cohen R & Chalumeau M, *Cochrane Database Syst Rev*, 2016 (2016).
130 Agarwal D K, *et al.*, *Biosens Bioelectron*, 195 (2022) 113647.
131 Holford T R J, Davis F & Higson S P J, *Biosens Bioelectron*, 34 (2012) 12.
132 Altug H, Oh S H, Maier S A & Homola J, *Nat Nanotechnol*, 17 (2022) 5.
133 Brolo A G, *Nat Photon*, 6 (2012) 709.
134 Mejía-Salazar J R & Oliveira O N, *Chem Rev*, 118 (2018) 10617.
135 Tseng M L, Jahani Y, Leitis A & Altug H, *ACS Photon*, 8 (2021) 47.
136 Seok T J, *et al.*, *Nano Lett*, 11 (2011) 2606.
137 Wu C, *et al.*, *Nat Mater*, 11 (2011) 69.
138 Sharma S, Kumari R, Varshney S K & Lahiri B, *Rev Phys*, 5 (2020) 100044.
139 Park S G & Jeong K H, *Int Conf Opt MEMS Nanophotonics*, (2014) 193.
140 Bontempi N, *et al.*, *Nanoscale*, 9 (2017) 4972.
141 Yavas O, Svedendahl M, Dobosz P, Sanz V & Quidant R, *Nano Lett*, 17 (2017) 4421.
142 Romano S, *et al.*, *Photon Res*, 6 (2018) 726.
143 Yesilkoy F, *et al.*, *Nat Photon*, 13 (2019) 390.
144 Ma B, *et al.*, *Electronics*, vol. 10 (2021) 1363.
145 Jahani Y, *et al.*, *Nat Commun*, 12 (2021) 4.
146 Elizarov M, Kivshar Y S & Fratalocchi A, *ACS Nanosci*, 2 (2022) 422.
147 Leitis A, *et al.*, *Sci Adv*, 5 (2019) 1.
148 Cambiasso J, König M, Cortés E, Schlücker S & Maier S A, *ACS Photon*, 5 (2018) 1546.
149 Romano S, *et al.*, *J Phys Chem C*, 122 (2018) 19738.
150 Cusano A, Consales M, Crescitelli A & Ricciardi A, *Lab-on-Fiber Technology*, 1st Edn, Cham: Springer International Publishing, 56 (2015).
151 Smythe E J, Dickey M D, Bao J, Whitesides G M & Capasso F, *Nano Lett*, 9 (2009) 1132.
152 Yang X, *et al.*, *Opt Express*, 20 (2012 24030.
153 Kostovski G, White D J, Mitchell A, Austin M W & Stoddart P R, *Biosens Bioelectron*, 24 (2009) 1531.
154 Kang S, Joe H E, Kim J, Jeong Y, Min B K & Oh K, *Appl Phys Lett*, 98 (2011) 96.
155 Consales M, Ricciardi A, Crescitelli A, Esposito E, Cutolo A & Cusano A, *ACS Nano*, 6 (2012) 3163.
156 Principe M, *et al.*, *Light Sci Appl*, 6 (2017) 16226.
157 Savinov V & Zheludev N I, *Appl Phys Lett*, 111 (2017) 091106.
158 Hahn V, Kalt S, Sridharan G M, Wegener M & Bhattacharya S, *Opt Express*, 26 (2018) 33148.
159 Novoselov K S, Mishchenko A, Carvalho A & Neto A H C, *Science*, 353 (2016) 9439.
160 Dereshgi S A, *et al.*, *Nat Commun*, 11 (2020) 5771.
161 Grosso G, *et al.*, *Nat Commun*, 8 (2017) 705.
162 Hill E W, Vijayaragahvan A & Novoselov K, *IEEE Sens J*, 11 (2011) 3161.
163 Du W, *et al.*, *Laser Photon Rev*, 14 (2020) 2000271.
164 Zhu L, *et al.*, *Light Sci Appl*, 5 (2016) 16052.
165 Ansari N, Mohebbi E & Gholami F, *Appl Phys B*, 126 (2019) 3.
166 Koppens F H L, Mueller T, Avouris P, Ferrari A C, Vitiello M S & Polini M, *Nat Nanotechnol*, 9 (2014) 780.
167 Xiao S, Zhu X, Li B -H & Mortensen N A, *Front Phys*, 11 (2016) 117801.
168 Dai S, *et al.*, *Science*, 343 (2014) 1125.
169 Ha D T Thuy, D T, Hoa V T, Van T T T & Viet N A, *J Phys Conf Ser*, 865 (2017) 12007.
170 Geim A K & Novoselov K S, *Nanoscience and Technology: A Collection of Reviews from Nature Journals*, Co-Published with Macmillan Publishers Ltd, UK, (2009) 11.
171 Banszerus L *et al.*, *2D Mater*, 4 (2017) 25030.
172 Lv R, *et al.*, *Acc Chem Res*, 48 (2015) 56.
173 Butler S Z, *et al.*, *ACS Nano*, 7 (2013) 2898.
174 Manzeli S, Ovchinnikov D, Pasquier D, Yazyev O V & Kis A, *Nat Rev Mater*, 2 (2017) 17033.
175 Bhimanapati G R, *et al.*, *ACS Nano*, 9 (2015) 11509.
176 Wang G, *et al.*, *Rev Mod Phys*, 90 (2018) 21001.
177 Jariwala D, Sangwan V K, Lauhon L J, Marks T J & Hersam M C, *ACS Nano*, 8 (2014) 1102.
178 Khurgin J B, *Nat Nanotechnol*, 10 (2015) 2.
179 Kuznetsov A I, Miroshnichenko A E, Brongersma M L, Kivshar Y S & Luk'yanchuk B, *Science*, 354 (2016) 2472.
180 Nair R R, *et al.*, *Science*, 320 (2008) 1308.
181 Han T-H, Kim H, Kwon S-J & Lee T-W, *Mater Sci Eng R Rep*, 118 (2017) 1.
182 Pandya A, Sorathiya V & Lavadiya S, Graphene-Based Nanophotonic Devices, in *Recent Advances in Nanophotonics - Fundamentals and Applications*, Intech Open, 2020.
183 Wang R, Ren X-G, Yan Z, Jiang L-J, Sha W E I & Shan G-C, *Front Phys*, 14 (2018) 13603.
184 Liu Y, Zhong R, Lian Z, Bu C & Liu S, *Sci Rep*, 8 (2018) 2828.
185 Wang X, Duan J, Chen W, Zhou C, Liu T & Xiao S, *Phys Rev B*, 102 (2020) 15543.
186 Sang T, Dereshgi S A, Hadibrata W, Tanriover I & Aydin K, *Nanomaterials*, 11 (2021) 484.
187 Yang C, Sang T, Li S, Wang Y, Cao G & Hu L, *J Opt Soc Am B*, 39 (2022) 2531.
188 Cai Y, Liu X, Zhu K, Wu H & Huang Y, *J Quant Spectrosc Radiat Trans*, 283 (2022) 108150.
189 Rastogi R, Foli E A D, Vincent R, Adam P-M & Krishnamoorthy S, *ACS Appl Mater Interfaces*, 13 (2021) 32653.

190 Nong J, *et al.*, *Small*, 17 (2021) 2004640.
191 Cao S, Wang Q, Gao X, Zhang S, Hong R & Zhang D, *AIP Adv*, 11 (2021) 85123.
192 Gao F, *et al.*, *Nanomaterials*, 11 (2021) 2032.
193 Parizi M S, Salemizadehparizi F, Zarasvand M M, Abdolhosseini S, Bahadori-Haghighi S & Khalilian A, *IEEE Sens J*, 22 (2022) 2037.
194 Sun G, Peng S, Zhang X & Zhu Y, *Nanomaterials*, 10 (2020) 1064,
195 Xiao S, *et al.*, *J Phys D Appl Phys*, 52 (2019) 385102.
196 Liu G-D, Zhai X, Xia S -X, Lin Q, Zhao C-J & Wang L-L, *Opt Express*, 25 (2017) 26045.
197 Argyropoulos C, *Opt Express*, 23 (2015) 23787.
198 Liu T, Wang H, Zhou C, Jiang X & Xiao S, *J Phys D Appl Phys*, 53 (2020) 505105.
199 Zhou Y *et al.*, *Nat Nanotechnol*, 12 (2017) 856.
200 Molas M R, *et al.*, *2D Mater*, 4 (2017) 21003.
201 Tan Q-H & Zhang J, *Sci China Mater*, 61 (2018) 1245.
202 Cihan A F, Curto A G, Raza S, Kik P G & Brongersma M L, *Nat Photon*, 12 (2018) 284.
203 Bucher T, *et al.*, *ACS Photon*, 6 (2019) 1002.
204 Lepeshov S, Krasnok A & Alù A, *Nanotechnology*, 30 (2019) 254004.
205 Lepeshov S, *et al.*, *ACS Appl Mater Interfaces*, 10 (2018) 16690.
206 Beal A R & Hughes H P, *J Phys C Solid State Phys*, 12 (1979) 881.
207 Verre R, Baranov D G, Munkhbat B, Cuadra J, Käll M & Shegai T, *Nat Nanotechnol*, 14 (2019) 679.
208 Weber T, *et al.*, *arXiv Prepr. arXiv2209.01944*, (2022) 1.
209 Hong Q, X Chen, Zhang J, Zhu Z, Qin S & Yuan X, *Nanoscale*, 11 (2019) 23149.
210 Löchner F J F, *et al.*, *Opt Express*, 27 (2019) 35475.
211 Dasgupta A, Gao J & Yang X, *Nano Lett*, 19 (2019) 6511.
212 Guddala S, Bushati R, Li M, Khanikaev A B & Menon V M, *Opt Mater Express*, 9 (2019) 536.
213 Bareza N J, *et al.*, *ACS Photon*, 9 (2022) 34.
214 Cao S, Jin Y, Dong H, Guo T, He J & He S, "*J Phys Mater*, 4 (2021) 35001.
215 Kioseoglou G, Hanbicki A T, Currie M, Friedman A L, Gunlycke D & Jonker B T, *Appl Phys Lett*, 101 (2012) 221907.
216 Korzeb K, Gajc M & Pawlak D A, *Opt Express*, 23 (2015) 25406.
217 Yadav A, Kumari R, Varshney S K & Lahiri B, *Opt Express*, 29 (2021) 33171.
218 Gigli C & Leo G, *Opto-Electronic Adv*, 5 (2022) 210093.
219 Bar-David J & Levy U, *Nano Lett*, 19 (2019) 1044.
220 Jin B & Argyropoulos C, *Phys Rev Appl*, 13 (2020) 1.
221 Kruk S S, *et al.*, *Nat Photon*, 16 (2022) 561.
222 Jha P K, Ni X, Wu C, Wang Y & Zhang X, *Phys Rev Lett*, 115 (2015) 025501.
223 Aharonov Y, Albert D Z & Vaidman L, *Phys Rev Lett*, 60 (1988) 1351.
224 Chen S, Zhou X, Mi C, Liu Z, Luo H & Wen S, *Appl Phys Lett*, 110 (2017) 161115.
225 Biehs S A & Agarwal G S, *Phys Rev A*, 96 (2017) 022308.
226 Jha P K, Shitrit N, Kim J, Ren X, Wang Y & Zhang X, *ACS Photon*, 5 (2018) 971.
227 Stav T, *et al.*, *Science*, 361 (2018) 1101.
228 Wang K, *et al.*, *Science*, 361 (2018) 1104.
229 Bub J, *Philos Phys*, (2007) 555.
230 S Lung, *et al.*, *ACS Photon*, 7 (2020) 3015.
231 Georgi P, *et al.*, *Light Sci Appl*, 8 (2019) 70.